scientific reports

Check for updates

OPEN

Bi-exponential diffusion-weighted imaging for differentiating high-grade gliomas from solitary brain metastases: a VOI-based histogram analysis

Yifei Su[1], Junhao Wang[1], Jinxia Guo[2], Xuanchen Liu[1], Xiaoxiong Yang[1], Rui Cheng[1], Chunhong Wang[1], Cheng Xu[3], Yexin He[3] & Hongming Ji[1✉]

This study investigated the use of bi-exponential diffusion-weighted imaging (DWI) combined with structural features to differentiate high-grade glioma (HGG) from solitary brain metastasis (SBM). A total of 57 patients (31 HGG, 26 SBM) who underwent pre-surgical multi-b DWI and structural MRI (T1W, T2W, T1W + C) were included. Volumes of interest (VOI) in the peritumoral edema area (PTEA) and enhanced tumor area (ETA) were selected for analysis. Histogram features of slow diffusion coefficient (D_{slow}), fast diffusion coefficient (D_{fast}), and perfusion fraction (frac) were extracted. Results showed that HGG patients had higher skewness of D_{fast} ($P = 0.022$) and frac ($P = 0.077$), higher kurtosis of D_{slow} ($P = 0.019$) and frac ($P = 0.025$), and lower entropy of D_{slow} ($P = 0.005$) and frac ($P = 0.001$) within the ETA. Additionally, HGG exhibited lower mean frac in both ETA ($P = 0.007$) and PTEA ($P = 0.017$). Combining skewness of frac in ETA with clear tumor margin enhanced diagnostic performance, achieving an optimal AUC of 0.79. These findings suggest that histogram analysis of diffusion and perfusion characteristics in ETA and structural features can effectively differentiate HGG from SBM.

Keywords Diffusion, Perfusion, Diffusion-weighted imaging, High-grade glioma, Solitary brain metastasis

Abbreviations

ADC	Apparent diffusion coefficient
CBV	Cerebral blood volume
D_{fast}	Fast diffusion coefficient
DWI	Diffusion-weighted imaging
D_{slow}	Slow diffusion coefficient
DSC	Dynamic susceptibility contrast
ETA	Enhanced tumor area
Frac	Perfusion fraction
GBM	Glioblastoma multiforme
HGG	High-grade glioma
PTEA	Peritumoral edema area
ROC	Receiver operator curves
SBM	Solitary brain metastasis
T1W	T1 weighted
T1W + C	Contrast-enhanced T1 weighted
T2W	T2 weighted
VOI	Volume of interest

[1]The Neurosurgery Department of Shanxi Provincial People's Hospital, Shanxi Medical University, Taiyuan 030012, Shanxi, People's Republic of China. [2]GE Healthcare, Beijing, People's Republic of China. [3]The Radiology Department of Shanxi Provincial People's Hospital, Taiyuan 030012, Shanxi, People's Republic of China. ✉email: hongmingj@sina.com

High-grade glioma (HGG) and brain metastasis are prevalent malignant neoplasms associated with substantial morbidity and mortality[1–3]. Differentiating a solitary brain metastasis (SBM) from an HGG has important prognostic and therapeutic implications.

HGG is commonly managed through surgical intervention followed by the Stupp protocol[4]. Brain metastases, which can present as single or multiple enhancing lesions, necessitate comprehensive whole-body staging[5]. Current treatment options for SBM include surgery or gamma-knife surgery and whole-brain radiation therapy[6,7]. Open surgical procedures are recommended for SBM patients with intractable intracranial hypertension, obstructive hydrocephalus, tumor apoplexy, and similar emergent situations[8]. However, considering that both HGG and SBM typically exhibit distinct imaging characteristics, including well-defined, ring-enhancing lesions in contrast-enhanced T1-weighted (T1W + C) imaging and high signal peritumoral edema in T2-weighted (T2W) imaging[9], diagnosis may be challenging. Also, individuals with extracranial malignancies may develop gliomas[10], which further complicates decision-making. Moreover, the incidence of geriatric glioma has been on the rise, challenging the notion that older individuals are more prone to developing brain metastases[11]. Furthermore, the clinical manifestations of HGG and SBM share similarities, such as secondary epilepsy, functional impairment, and intracranial hypertension, which contribute to the complexity of distinguishing between the two entities, both radiologically and clinically[12].

Primary malignancy history, multiple lesions, and the combined localization of grey–white substances can help diagnose brain metastasis. Traditional morphological analyses, including assessments of tumor parenchymal or peritumoral edema volume, midline shift, and enhancement pattern in various conventional magnetic resonance sequences, have proven ineffective in differentiating HGG from SBM[13,14]. On the other hand, histogram and texture analysis techniques based on diffusion-weighted imaging (DWI) and diffusion kurtosis imaging have shown promising results in differentiating HGG from SBM. This method can reflect the distribution of diffusion within the tumor or edema area[15,16]. Furthermore, conventional perfusion MR studies utilizing dynamic susceptibility contrast (DSC), dynamic contrast-enhanced imaging, and arterial spin labeling have demonstrated excellent diagnostic performance in distinguishing these tumor types[17,18]. However, research focusing on analyzing perfusion histogram features is lacking.

Bi-exponential analysis of DWI data enables the simultaneous assessment of molecular water diffusion at high-b values and the microcirculation of blood capillaries associated with perfusion at low-b values (b < 200 s/mm^2)[19]. Previous studies have suggested that this imaging approach can accurately differentiate high-grade from low-grade gliomas[20]. In this study, we explored the potential of bi-exponential analysis of DWI data in differentiating HGG and SBM in both enhanced tumor area (ETA) and peritumoral edema area (PTEA) through histogram analysis combined with structural features.

Results

Clinical characteristics and structural differences between HGG and SBM

Among initially enrolled 81 patients with brain metastasis and 145 patients with HGG, 87 with incomplete image data, 11 with poor image quality, 25 with tumor tumors located below the tentorium cerebelli, and 46 with more than one tumor lesion above the tentorium cerebelli were excluded. The final cohort consisted of 31 patients with HGG (Table S1), with a mean age of 58.6 ± 19.37, and 26 patients with SBM (Table S2), with a mean age of 59.69 ± 11.59 (Fig. 1).

There were no significant differences in age or gender distribution between the HGG and SBM groups. However, SBM exhibited a significantly cleaner tumor margin than HGG ($P = 0.017$). No significant differences were observed between the two groups regarding tumor location, edema degree, or enhancement pattern. Detailed information is provided in Table 1.

Parametric value comparison between HGG and SBM

The histogram features of ETA and PTEA in patients with HGG) and solitary brain SBM are shown in Table 2. A significantly higher skewness of D_{fast} (1.1 ± 0.32 in HGG, 0.81 ± 0.54 in SBM, $P = 0.022$) and frac (1.02 ± 0.51 in HGG, 0.6 ± 0.61 in SBM, $P = 0.077$), as well as higher kurtosis of D_{slow} (3.9 ± 1.22 in HGG, 3.39 ± 1.29 in SBM, $P = 0.019$) and frac (5.39 ± 2.07 in HGG, 4.51 ± 2.72 in SBM, $P = 0.025$) were observed for patients with HGG compared to SBM. Additionally, significantly lower entropy of D_{slow} (3.86 ± 0.21 in HGG, 4.01 ± 0.22 in SBM, $P = 0.005$) and frac (3.51 ± 0.3 in HGG, 3.78 ± 0.28 in SBM, $P = 0.001$) were observed in ETA for HGG. In addition, the mean of frac in both ETA (21.29 ± 4.02 in HGG, 25.09 ± 6.03 in SBM, $P = 0.007$) and PTEA (25.47 ± 4.46 in HGG, 28.37 ± 4.22 in SBM, $P = 0.017$) was significantly lower in HGG compared to SBM. Furthermore, there was a significant difference between the groups in the 10th percentile of frac (10.99 ± 2.56 in HGG, 13.87 ± 4.66 in SBM, $P = 0.009$) in ETA. Representative images and histograms of D_{fast}, D_{slow}, and frac in the ETA volume of interest (VOI) for a patient with HGG (Fig. 2) and another with SBM (Fig. 3) are shown below.

Evaluating the performance with structural and histogram features

Through single-factor regression analysis, skewness of D_{fast} (OR = 0.22, 95%CI 0.06–0.80, $P = 0.022$) and frac (OR = 0.24, 95% CI 0.08–0.74, $P = 0.013$), the entropy of D_{slow} (OR = 26.20, 95% CI 1.71–402.6, $P = 0.019$) and frac (OR = 22.32, 95% CI 2.92–170.7, $P = 0.003$), and mean of frac (OR = 1.16, 95% CI 1.03–1.31, $P = 0.014$) in ETA, mean of frac (OR = 1.17, 95% CI 1.02–1.35, $P = 0.025$) in PTEA, and clear tumor margin on T2W (OR = 4.30, 95% CI 1.39–13.26, $P = 0.011$) were identified as associated factors for differentiating HGG from SBM (Table 3).

When combined with clear tumor margin on T2W imaging, the binary logistic regression analysis showed that skewness of D_{fast} (OR = 0.25, 95%CI 0.07–0.94, $P = 0.040$) and frac (OR = 0.21, 95% CI 0.06–0.68, $P = 0.009$), entropy of D_{slow} (OR = 21.77, 95% CI 1.21–392.7, $P = 0.037$) and frac (OR = 17.44, 95% CI 2.14–142.3, $P = 0.008$),
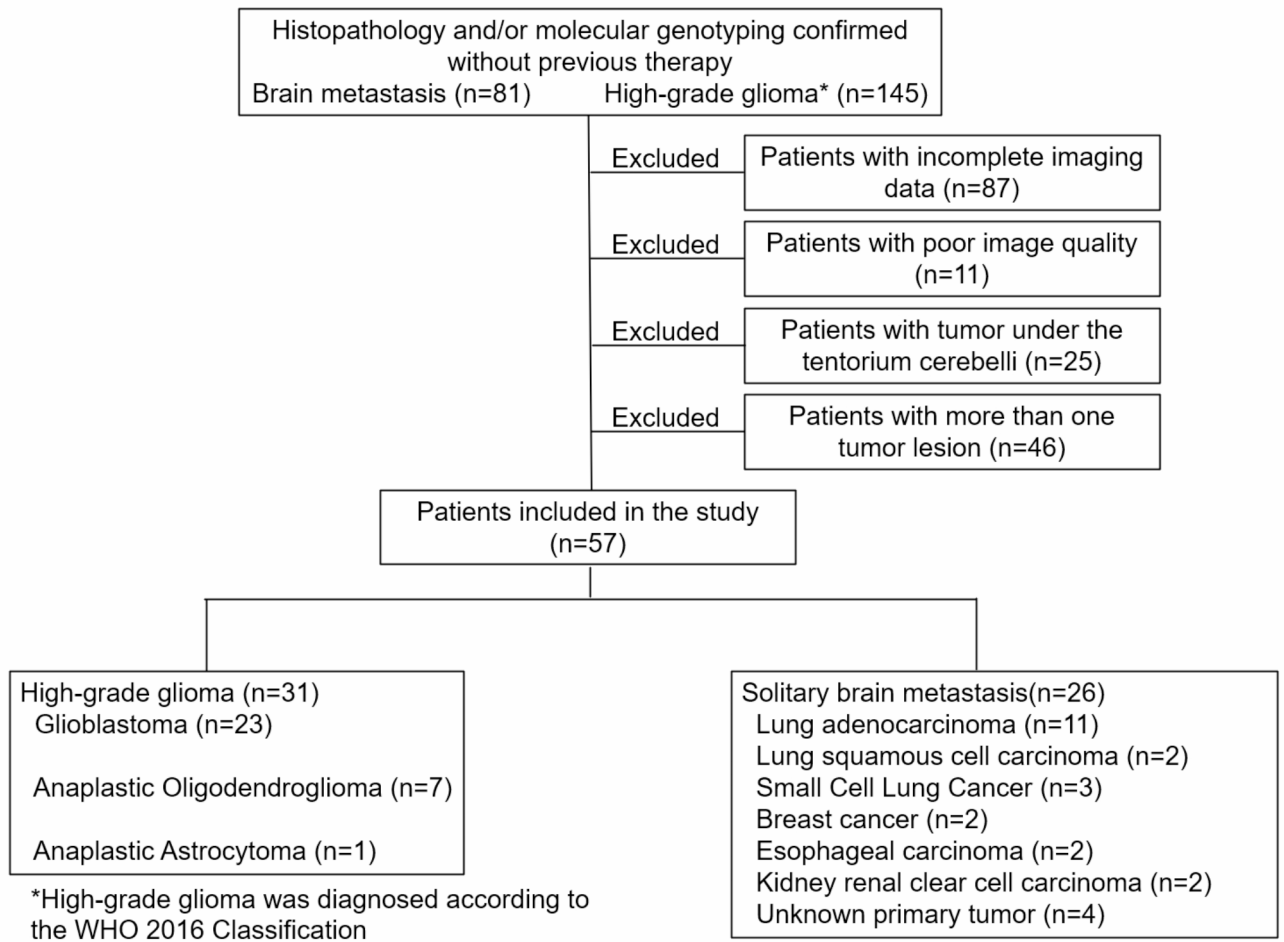
Fig. 1. Study flow chart.

	HGG ($n = 31$)	SBM ($n = 26$)	P
Demographics			
Age (year)	58.61 ± 9.37	59.69 ± 11.59	0.356
Gender (male/female)	18/13	10/16	1
Tumor location			0.183
Sub-cortex	13	16	
Deep white matter	18	10	
T2 margin			0.017*
Blurred margin	19	7	
Well-defined margin	12	19	
Edema degree			0.63
Mild	9	6	
Moderate	7	6	
Severe	15	14	
Enhancement pattern			
Non-enhanced	1	0	0.901
Focal	5	0	
Diffuse	9	15	
Ring-like	16	11	

Table 1. Clinical characteristics and morphological features comparison between HGG and SBM. *$P < 0.05$.

	Mean	Entropy	Skewness	Kurtosis	10th percentile	90th percentile
ETA						
D_{fast} (×10^{-4}mm^2/s)						
HGG	41.63 ± 3.34	3.62 ± 0.37	1.1 ± 0.32	5.48 ± 1.91	28.03 ± 3.71	58.54 ± 8.52
SBM	42.22 ± 5.73	3.8 ± 0.42	0.81 ± 0.54	4.78 ± 2.2	26.61 ± 6.12	59.99 ± 11.66
P	0.641	0.092	0.022*	0.082	0.628	0.598
D_{slow} (×10^{-4}mm^2/s)						
HGG	9.27 ± 1.1	3.86 ± 0.21	0.73 ± 0.43	3.9 ± 1.22	6.89 ± 0.89	11.96 ± 1.42
SBM	9.38 ± 1.37	4.01 ± 0.22	0.56 ± 0.53	3.39 ± 1.29	7.08 ± 1.13	11.94 ± 1.8
P	0.748	0.005*	0.450*	0.019*	0.469	0.960
frac (%)						
HGG	21.29 ± 4.02	3.51 ± 0.3	1.02 ± 0.51	5.39 ± 2.07	10.99 ± 2.56	33.08 ± 6.87
SBM	25.09 ± 6.03	3.78 ± 0.28	0.6 ± 0.61	4.51 ± 2.72	13.87 ± 4.66	36.7 ± 8.61
P	0.007*	0.001*	0.007*	0.025*	0.009*	0.088
PTEA						
D_{fast} (×10^{-4}mm^2/s)						
HGG	37.73 ± 2.99	3.29 ± 0.5	1.69 ± 0.67	8.91 ± 4.75	26.73 ± 3	51.93 ± 9.11
SBM	37.9 ± 3.75	3.3 ± 0.66	1.58 ± 0.64	8.83 ± 4.63	25.82 ± 4.65	53.17 ± 12.56
P	0.793	0.769	0.530	0.943	0.685	0.943
D_{slow} (×10^{-4}mm^2/s)						
HGG	11.08 ± 1.44	4.06 ± 0.32	0.13 ± 0.46	2.9 ± 1.79	7.93 ± 0.95	14.18 ± 1.86
SBM	11.32 ± 1.31	4.03 ± 0.23	0.03 ± 0.41	2.72 ± 1.05	8.25 ± 1.17	14.22 ± 1.68
P	0.709	0.254	0.377	0.981	0.264	0.88
frac (%)						
HGG	25.47 ± 4.46	3.32 ± 0.25	0.55 ± 0.75	6.26 ± 3.62	14.99 ± 3.61	34.73 ± 5.47
SBM	28.37 ± 4.22	3.39 ± 0.36	0.51 ± 0.71	5.55 ± 2.55	17.59 ± 4.2	38.81 ± 7.36
P	0.017*	0.327	0.864	0.377	0.059	0.059

Table 2. Comparison of parametric values in the volume of interest between HGG and SBM. ETA: enhanced tumor area; PTEA: peritumor edema area; * $P < 0.05$.

and mean of frac (OR = 1.15, 95% CI 1.01–1.30, $P = 0.032$) in ETA, as well as mean of frac (OR = 1.18, 95% CI 1.01–1.37, $P = 0.034$) in PTEA, showed significant differences (Table 3). Among these factors, the entropy of frac in ETA exhibited the best performance for differentiation, with an AUC of 0.74 (sensitivity = 0.88, specificity = 0.55) in ROC analysis (Table 4; Fig. 4A). Furthermore, integrating clear tumor margin on T2W and skewness of frac in ETA improved the performance, with an optimal AUC of 0.79 (sensitivity = 0.81, specificity = 0.71) (Table 4; Fig. 4B). Moreover, calibration analysis using a bootstrap resampling method showed a good correlation between apparent and bias-corrected multivariate logistic regression in all the binary logistic regression models (Figure S1).

Discussion

By employing histogram analysis in combination with the structural feature, we examined the accuracy of DWI in distinguishing HGG from SBM. The inclusion of DWI parametric values combined with the presence of a clear tumor margin in T2W imaging improved the differentiation process. The significant differences in histogram features of D_{fast}, D_{slow}, and frac within ETA suggested distinct diffusion and perfusion heterogeneity between HGG and SBM.

The accurate differentiation between HGG and SBM is crucial for patient management and can significantly impact clinical outcomes. While conventional structural MR imaging may not provide sufficient distinguishing features between HGG and SBM[9], advanced diffusion, perfusion, and molecular MR techniques have been explored either individually or in combination with other models[21–23]. Previous studies have predominantly employed region of interest (ROI) based methods for analysis, with limited utilization of VOI-based approaches[24,25]. In this study, we adopted a VOI-based histogram analysis to investigate the diffusion and perfusion differences between HGG and SBM within the enhanced tumor area and the peritumoral edema area. This approach was superior to localized hotspot techniques regarding interobserver agreement and diagnostic accuracy, as supported by previous studies[24].

In the ETA, HGG showed significantly higher skewness (D_{fast}, frac) and kurtosis (D_{slow}, frac) while demonstrating significantly lower entropy (D_{slow}, frac) and mean (frac) compared to SBM. The higher kurtosis indicated that the distribution of water diffusion and microvascular perfusion in the enhanced tumor region was more concentrated in HGG, and the lower entropy in HGG suggested a lower degree of molecular disorder in the diffusion and perfusion patterns, as shown in Fig. 2 (HGG) and Fig. 3 (SBM). Moreover, the significantly higher kurtosis and skewness in HGG indicated the presence of more extreme perfusion values, implying that
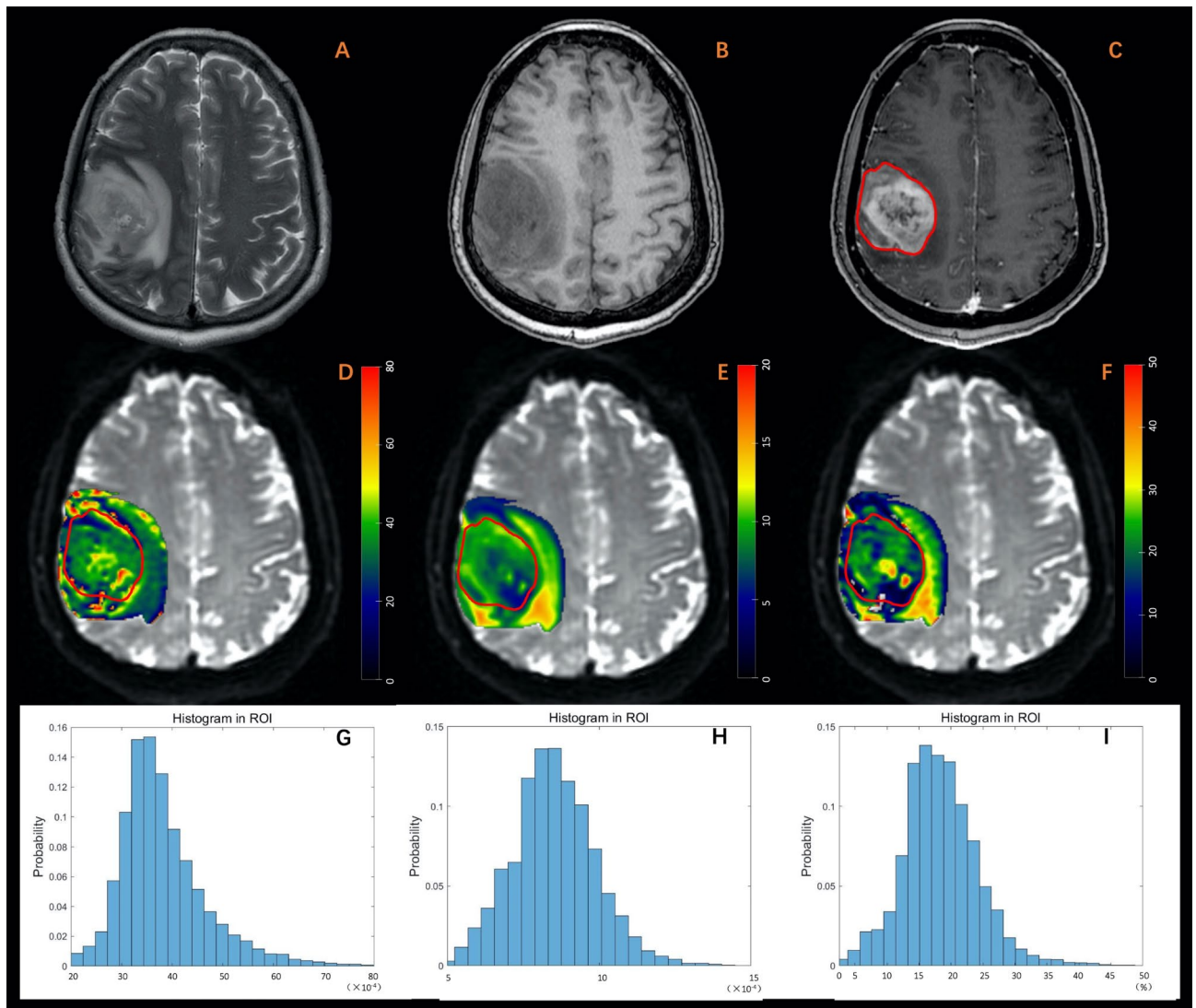
Fig. 2. A 63-year-old male diagnosed with glioblastoma. (**A**) T2W imaging. (**B**) T1W imaging. (**C**) Contrast-enhanced T1W imaging. (**D**) D_{fast} ($\times 10\text{-}4mm^2/s$). (**E**) D_{slow} ($\times 10\text{-}4mm^2/s$). (**F**) frac (%). (**G-I**) Histogram plot of Dfast, Dslow, and frac of the enhanced tumor area. The MRI examination revealed an irregular lesion in the sub-cortex of the right frontal lobe, characterized by a blurred margin. The lesion exhibited diffuse enhancement, marked in red, along with hyper-intensity on T2-weighted imaging and hypo-intensity on T1-weighted imaging. Peritumoral edema was also observed. Parametric values obtained from histogram analysis of the enhanced tumor area are as follows: D_{fast}: mean: 37.98, entropy: 3.19, skewness: 1.15, kurtosis: 6.60. D_{slow}: mean: 8.52, entropy: 3.68. skewness: 0.33, kurtosis: 3.60, frac: mean: 18.46, entropy: 3.07, skewness: 0.68, kurtosis: 5.06.

micro-vessel characteristics influence microvascular perfusion in most ETA. A study conducted by Heynold et al. demonstrated that glioblastomas exhibit higher levels of neovascularization activity and metabolic rate of oxygen in the ETA compared to brain metastasis[22]. However, based on our findings of significantly lower mean and 10th percentile of frac in the ETA, we can conclude that HGG exhibits a predominantly poorer microvascular perfusion than SBM. This difference in perfusion could be due to the attenuation of blood supply caused by microscopic intravascular thrombosis[26]. HGG exhibits a pronounced capacity for neovascularization; nevertheless, most of these newly formed blood vessels are functionally inert[26]. These findings highlight the distinct diffusion and perfusion characteristics between HGG and SBM in ETA, shedding light on the underlying pathophysiological differences between the two tumor types.

In their recent study, Poulon et al.[27] utilized real-time fresh human brain tumor samples imaging with endogenous fluorophores and observed higher microvascular density in metastasis compared to glioblastoma multiforme (GBM) and healthy tissues. They also found that the solid tumor component in GBM samples exhibited a highly disordered tumor cell architecture with microvascular growth, which could help explain the higher kurtosis values of D_{slow} and frac observed in our study. In the diffusion study of GBM and SBM differential diagnosis, Romano et al.[25] found significantly lower mean apparent diffusion coefficient (ADC) values in GBM.
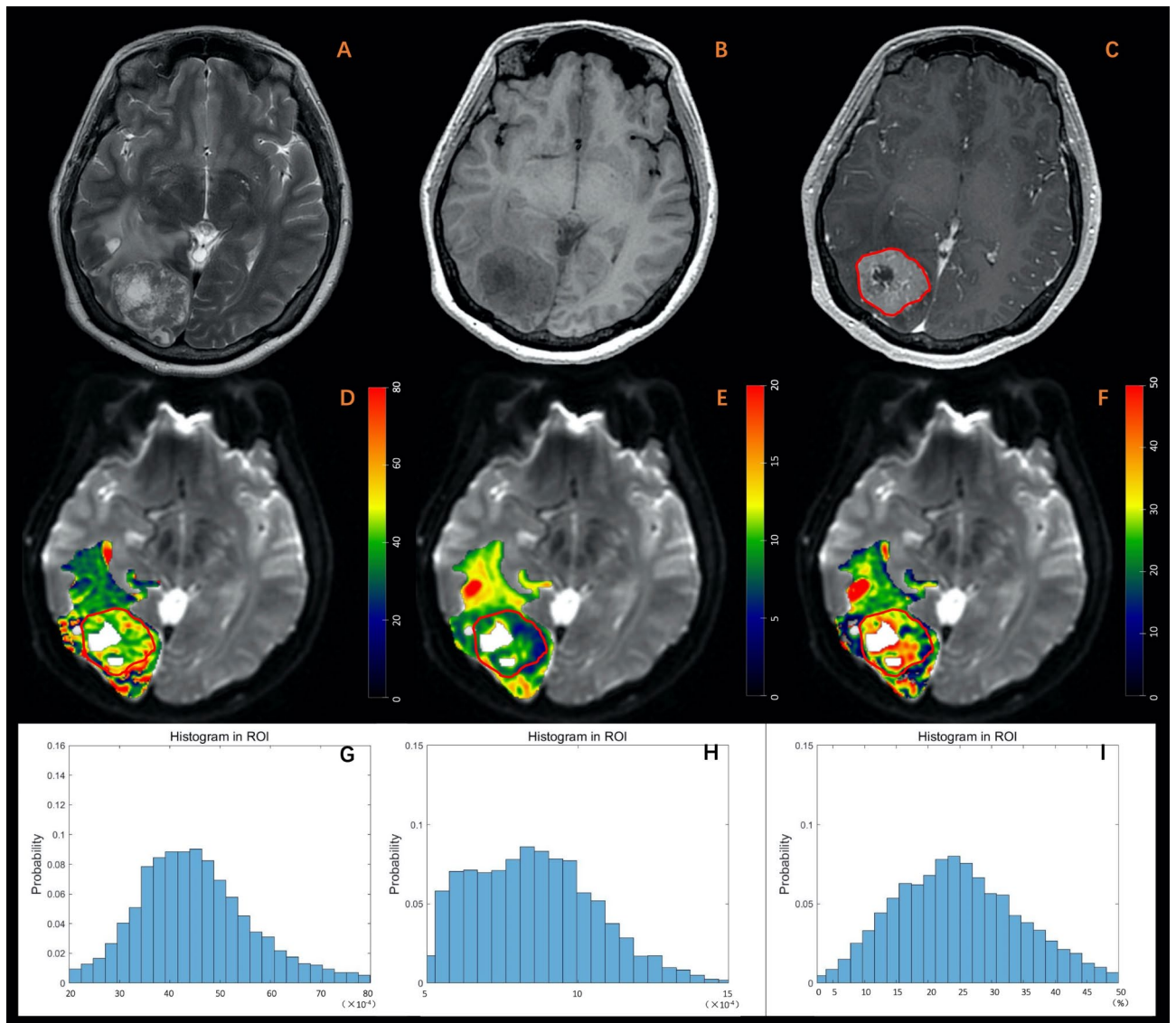
Fig. 3. A 34-year-old female diagnosed with brain metastasis originating from breast cancer. (**A**) T2W imaging. (**B**) T1W imaging. (**C**) Contrast-enhanced T1W imaging. (**D**) D_{fast} ($\times 10\text{-}4mm^2/s$). (**E**) D_{slow} ($\times 10\text{-}4mm^2/s$). (**F**) frac (%). (**G-I**) Histogram plot of Dfast, Dslow, and frac of the enhanced tumor area. The MRI examination revealed an irregular lesion with a well-defined margin in the sub-cortex of the right occipital lobe. The lesion exhibited diffuse enhancement, marked in red, and appeared hyper-intense on T2-weighted imaging, hypo-intense on T1-weighted imaging, and was accompanied by peritumoral edema. Additionally, central necrosis was observed within the lesion. Parametric values obtained from histogram analysis of the enhanced tumor area are as follows: D_{fast}: mean: 45.38, entropy: 3.80, skewness: 0.70, kurtosis: 4.42; D_{slow}: mean: 8.55, entropy: 4.09, skewness: 0.47, kurtosis: 2.85; frac: mean: 25.15, entropy: 3.76, skewness: 0.49, kurtosis: 3.31.

Moreover, Chiang et al.[28] reported higher ADC values in metastasis compared to HGG. On the other hand, Tsougos et al. found no significant difference in ADC and fractional anisotropy between the two tumor groups[29]. It is important to note that our study employed a VOI-based analysis and included HGGs in addition to GBM, whereas the mentioned studies utilized hotspot methods[28,29], which could account for the observed discrepancies. In a DSC perfusion MRI study using histogram analysis, Qin et al. demonstrated that GBM exhibited a more heterogeneous distribution of blood perfusion in the enhancing tumor area than metastasis[24]. However, the mean value of absolute cerebral blood volume (CBV) did not show a significant difference, which aligns with previous research highlighting the limitations of relative CBV[30]. Our study focusing on micro-vessel perfusion revealed higher heterogeneity and significantly lower mean values in HGG compared to SBM. These findings suggest that micro-vessel perfusion parameters hold promise as potential discriminative factors warranting further investigation. Previous studies using DSC perfusion MRI have consistently shown higher perfusion values in the PTEA of GBM compared to brain metastasis[28,29,31]. Additionally, there is a decreasing gradient of

Univariate logistic regression	OR	(95% CI)	P	Binary logistic regression	OR	(95% CI)	P
ETA							
Dfast_skewness	0.22	(0.06,0.80)	0.022*	Dfast_skewness	0.25	(0.07,0.94)	0.040*
				+clear_t2_margin	3.93	(1.21,12.72)	0.022*
Dslow_entropy	26.20	(1.71,402.6)	0.019*	Dslow_entropy	21.77	(1.21,392.7)	0.037*
				+clear_t2_margin	3.91	(1.20,12.75)	0.024*
Dslow_kurtosis	0.71	(0.44,1.13)	0.146				
frac_mean	1.16	(1.03,1.31)	0.014*	frac_mean	1.15	(1.01,1.30)	0.032*
				+clear_t2_margin	3.64	(1.11,11.87)	0.032*
frac_entropy	22.32	(2.92,170.7)	0.003*	frac_entropy	17.44	(2.14142.30)	0.008*
				+clear_t2_margin	3.48	(1.02,11.85)	0.046*
frac_skewness	0.24	(0.08,0.74)	0.013*	frac_skewness	0.21	(0.06,0.68)	0.009*
				+clear_t2_margin	5.43	(1.55,18.97)	0.008*
frac_kurtosis	0.84	(0.65,1.09)	0.190				
PTEA							
frac_mean	1.17	(1.02,1.35)	0.025*	frac_mean	1.18	(1.01,1.37)	0.034*
				+clear_t2_margin	4.34	(1.31,14.31)	0.016*
clear_t2_margin	4.30	(1.39,13.28)	0.011*				

Table 3. Univariate and binary logistic regression analysis. HGG: high-grade glioma; SBM: solitary brain metastasis; ETA: enhanced tumor area; PTEA: peritumor edema area. OR: odds ratio; 95% CI: 93% confidence interval; * $P < 0.05$.

	AUC (95% CI)	Sensitivity (95% CI)	Specificity (95% CI)	Accuracy (TN + TP)/(N + P)	PPV (TP/P)	NPV (TN/N)	Threshold
ETA							
Dfast_skewness	0.67 (0.52,0.83)	0.58 (0.38.0.77)	0.77 (0.61,0.90)	0.68 (39/57)	0.68 (15/22)	0.69 (24/35)	0.87
Dslow_entropy	0.71 (0.58,0.85)	0.88 (0.77,1.00)	0.55 (0.39,0.71)	0.70 (40/57)	0.62 (23/37)	0.85 (17/20)	3.85
frac_mean	0.71 (0.57,0.85)	0.58 (0.38,0.77)	0.87 (0.74,0.967)	0.74 (42/57)	0.79 (15/19)	0.71 (27/38)	24.74
frac_entropy	0.74 (0.61,0.87)	0.88 (0.73.1.00)	0.55 (0.39,0.71)	0.70 (40/57)	0.62 (23/37)	0.85 (17/20)	3.51
frac_skewness	0.72 (0.58,0.86)	0.54 (0.35,0.73)	0.90 (0.81,1.00)	0.74 (42/57)	0.82 (14/17)	0.70 (28/40)	0.52
PTEA							
frac_mean	0.65 (0.50,0.79)	0.62 (0.42,0.81)	0.65 (0.48,0.81)	0.63 (36/57)	0.59 (16/27)	0.67 (20/30)	27.29
clear_t2_margin	0.67 (0.55.0.79)	0.73 (0.54,0.88)	0.61 (0.42,0.77)	0.67 (38/57)	0.61 (19/31)	0.73 (19/26)	0.44
ETA							
Dfast_skewness +clear_t2_margin	0.76 (0.63,0.89)	0.77 (0.62,0.92)	0.68 (0.48,0.84)	0.72 (41/57)	0.67 (20/30)	0.78 (21/27)	0.44
Dslow_entropy +clear_t2_margin	0.76 (0.63,0.89)	0.65 (0.46,0.85)	0.81 (0.68,0.94)	0.74 (42/57)	0.74 (17/23)	0.74 (25/34)	0.54
frac_mean +clear_t2_margin	0.76 (0.63,0.89)	0.50 (0.31,0.69)	0.94 (0.84,1.00)	0.74 (42/57)	0.87 (13/15)	0.69 (29/42)	0.61
frac_entropy +clear_t2_margin	0.78 (0.66,0.90)	0.77 (0.62,0.92)	0.71 (0.55,0.87)	0.74 (42/57)	0.69 (20/29)	0.79 (22/28)	0.49
frac_skewness +clear_t2_margin	0.79 (0.67,0.91)	0.81 (0.65,0.92)	0.71 (0.55,0.87)	0.75 (43/57)	0.70 (21/30)	0.81 (22/27)	0.42
PTEA							
frac_mean +clear_t2_margin	0.75 (0.62,0.88)	0.85 (0.69,0.96)	0.58 (0.42.0.74)	0.70 (40/57)	0.63 (22/35)	0.82 (18/22)	0.36

Table 4. Univariate logistic regression and binary logistic regression performance in the differentiation of HGG and SBM. HGG: high-grade glioma; SBM: solitary brain metastasis; ETA: enhanced tumor area; PTEA: peritumor edema area. AUC: area under the curve; PPV: positive predictive value; NPV: negative predictive value. 95% CI: 95% confidence interval; TN: true negative; TP: true positive; N: negative; P: positive.
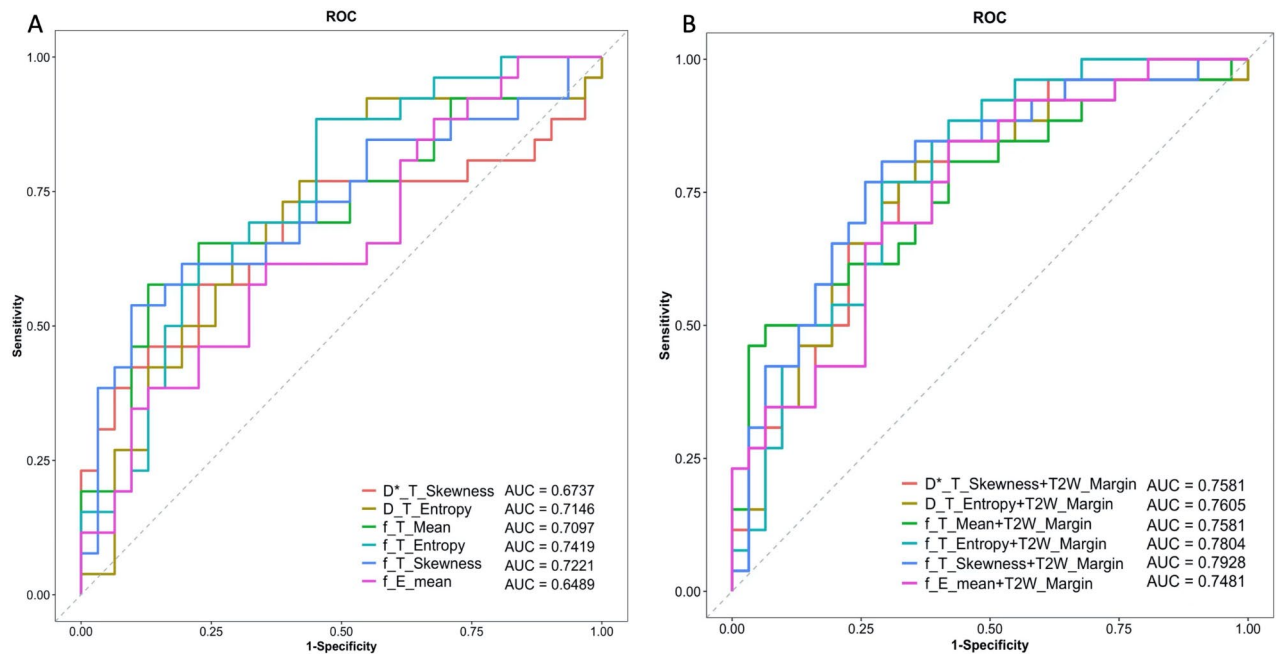
Fig. 4. The ROC curves for univariate (**A**) and binary (**B**) logistic regression analysis.

relative CBV values from the region adjacent to the enhancing solid lesion to the normal white matter in GBM, whereas this gradient is less pronounced in brain metastasis[25,32,33]. The differential growth patterns of GBM and metastasis, with GBM exhibiting infiltrative growth beyond the boundaries of the enhancing tumor core[34,35] and metastasis primarily expanding and causing vasogenic edema[36], contribute to the distinct microenvironments associated with these tumors. These variations in microenvironments can lead to differences in diffusion and perfusion characteristics. However, in this study, only the mean value of the frac parameter showed a significant distinction between GBM and metastasis in the PTEA. Interestingly, this parameter did not outperform other measurements in the ETA. The presence of a perfusion gradient within the PTEA and the utilization of a VOI-based analysis in our study may account for these findings. It is worth noting that the distribution of D_{fast}, D_{slow}, and frac varies among different lobes, and the localization of the edema area also differs across lobes, which could potentially impact the observed outcomes[37].

In this study, we included solitary brain metastases originating from various primary sites but mostly from lung, which is consistent with previous studies[17,38,39]. Among these, lung adenocarcinoma was the most prevalent histological subtype. In their analysis of the tumor and immune cell phenotypic composition in metastatic breast cancer, Kuett et al. highlighted significant heterogeneity both within individual patients and across different metastatic sites[40]. Research suggests that techniques like PET can assist in predicting the primary site of brain metastases[38], which implies that brain metastases originating from different primary sites may exhibit distinct perfusion or metabolic patterns, reflecting their varied biological behaviors. However, a meta-analysis by Fioni et al. involving 399 HGG and 232 SBM cases found that the relative CBV values in the central area of the tumor did not significantly differ between HGG patients and SBM/controls.[41] These findings highlight the need for further research with larger, more balanced cohorts to investigate whether metastases from different sites will lead to differences in imaging.

The DWI scanning protocol with 12 b-values ranging from 0 to 2000 s/mm^2 was adopted in our study, while data analysis was performed with a bi-exponential fitting model using b-values of 200 to 1200 s/mm^2. This range was selected because pseudo-diffusion from blood flow occurs at a faster rate than bulk-water diffusion, and diffusion signals below 200–400 s/mm^2 are predominantly influenced by perfusion-diffusion effects[42]. Our initial analysis revealed poor fitting when data points at b = 1500 and 2000 s/mm^2 were included (Figure S2). Currently, there is no universally standardized b-value protocol for multi-b DWI analysis, and different studies have used different b-value settings[43,44]. Han et al. reported significantly lower ADC values in the peritumoral region of HGG compared to SBM, with an AUC of 0.922 at b-values of 3000 s/mm^2 and 0.886 at 1000 s/mm^2 based on ROC analysis[45]. In our future work, we plan to investigate the potential of Cramer Rao Lower Bound analysis for selecting optimal b-values[46,47].

Advanced magnetic resonance techniques offer valuable insights into the diffusion, perfusion, and metabolism of different lesions, while histogram analysis provides additional information for understanding tumor pathogenesis. Furthermore, radiomics, genomics, and neural network can deepen investigations, providing advanced tools for tumor differentiation. For example, the model of neurite orientation dispersion and density imaging radiomics within the solid tumor area showed promising performance for preoperative discrimination between glioblastoma and SBM (AUC = 0.904)[48]. GoogLeNet performed better than previous methods at differentiating HGG from SBM both in core (external dataset, accuracy of 86.76%, sensitivity of

81.82%, specificity of 83.33%, and AUC of 0.866) and peritumoral edema area (external dataset, accuracy of 79.31%, sensitivity of 81.82%, specificity of 77.78% and AUC of 0.826)[49].

However, the higher-dimensional results from multi-omics can be challenging to interpret biologically, so there is a need for more practical and straightforward approaches that can be easily implemented in smaller medical facilities and time-limited clinical practice. In clinical settings, structural features are still widely utilized. Yamamoto et al.[50] evaluated the efficacy of an extensive peritumor hyperintense rim in differentiating metastatic brain tumors from GBM using contrast-enhanced Fast imaging employing steady-state acquisition and reported high sensitivity (0.95), specificity (0.95), and accuracy (0.93) compared to conventional MR-based tumor shape analysis. However, they did not provide the AUC value. Herein, we identified a clear tumor margin on T2W imaging as the only structural feature distinguishing HGG from SBM. Further ROC analysis revealed that when combined with the skewness of frac in the enhanced tumor region, it significantly improved the differentiation performance, yielding the highest AUC of 0.79 (sensitivity = 0.81, specificity = 0.71). Moreover, they included metastasis cases with multiple lesions (32.6%), which may have potentially exaggerated their findings. Another efficient tool for tumor differential diagnosis is the Artificial Intelligence-Assisted Decision-Making System[51]; however, bridging the gap between experimental research and regulatory standards requires further validation, standardization, and extensive clinical trials.

The present study has some limitations. First, the number of patients included was relatively small, and there was variability in the original metastasis lesions. Second, external verification was lacking as all patients were from one medical center. Third, detailed pathological information, such as immunohistochemical staining, cell distribution density, and micro-vessel density, was not utilized in this study, and incorporating these factors in future research could provide valuable insights and help validate the findings. In our next study, we plan to compare diffusion kurtosis between HGG and SBM and analysis using the Cramer Rao Lower Bound method to determine the most suitable b-values.

Methods

Study population

Patients who underwent MR examination between December 2020 and June 2022 were included in this retrospective study. The inclusion criteria were: (1) patients with histopathologically or molecularly genotyped HGG (according to the WHO 2016 Classification[52]) or brain metastasis; (2) patients who received no radiotherapy or who did not undergo surgical treatment before diagnosis; (3) age > 18 years old. The exclusion criteria were: (1) tumors located below the tentorium cerebelli; (2) presence of more than one tumor lesion above the tentorium cerebelli; (3) incomplete imaging data; (4) poor imaging quality, such as severe motion artifacts, significant cystic, hemorrhagic, or extensive tumor necrosis. The pathology tissue was acquired through a craniotomy or robotic-assisted biopsy surgery about one week after the MR scanning. The patient enrollment process is depicted in Fig. 1.

This study was conducted in accordance with the guidelines outlined in the Declaration of Helsinki and was approved by the institutional review board of Fifth Hospital of Shanxi Medical University/Shanxi Provincial People's Hospital, Taiyuan, Shanxi, P. R. China. Informed consent was waived due to the retrospective nature of the study.

Imaging data acquisition

The imaging protocol was performed in the following order: T2W, T1W, DWI, contrast injection, and T1W + C. All magnetic resonance scans were conducted using a 3.0T MR scanner (Discovery MR 750 W, GE Healthcare, Waukesha, WI, USA) equipped with a 24-channel head-neck coil, ensuring consistent positioning. Axial DWI imaging utilized 12 b-values (0, 20, 40, 80, 110, 150, 200, 400, 800, 1200, 1500, and 2000 s/mm^2) with corresponding acquisition times of 1, 1, 1, 1, 1, 1, 2, 2, 2, 2, and 4 s. The following parameters were used: repetition time/echo time (TR/TE) = 5400/90 ms, field of view (FOV) = 220 × 220 mm^2, matrix size = 110 × 110, slice thickness = 4.0 mm, number of slices = 24, gap = 1.0 mm, and acquisition time = 5 min and 28 s. Axial T2W imaging was performed using the following parameters: TR/TE = 7900/125 ms, FOV = 230 × 230 mm^2, matrix size = 380 × 380, slice thickness = 4.5 mm, number of slices = 30, gap = 5 mm, flip angle = 140°, and acquisition time = 2 minutes. For axial T1W imaging, the following parameters were used: TR/TE = 2500/24 ms, FOV = 230 × 230 mm^2, matrix size = 320 × 224, slice thickness = 4.0 mm, number of slices = 30, gap = 5 mm, flip angle = 110°, and acquisition time = 1 min and 19 s. T1W + C imaging employed the same parameters as T1W, and gadodiamide was power-injected at a rate of 2 ml/s, with dosages calibrated based on the patient's body weight (0.2 ml/kg). The scan began 3–5 min after the injection. Images were acquired sequentially in the axial, sagittal, and coronal planes. The total imaging time was approximately 20 min.

Volume of interest (VOI)

VOI for the PTEA and ETA were delineated by two experienced neuroradiologists with 20 and 25 years of experience, respectively. Consensus was reached between the radiologists during the delineation process, which was performed on a slice-by-slice basis using 3D-slicer software (version 4.10, available at https://www.slicer.org) referring to the T2W and T1W + C images for PTEA and ETA, respectively. We especially made sure to minimize the inclusion of calcifications, intra-tumor hemorrhage, cysts, and hyperintensity surrounding the ventricular system and skull base, as suggested by previous studies[53,54].

Bi-exponential analysis

For the calculation of the slow diffusion coefficient (D_{slow}), fast diffusion coefficient (D_{fast}), and perfusion fraction (frac) within the VOI, an in-house program was developed in MATLAB 2018b. The program utilized the bi-exponential fitting approach defined by:

$$Sb = [frac \times exp(-b \times Dfast) + (1 - frac) \times exp(-b \times Dslow)] \times S0 \qquad (1)$$

where Sb and S0 represents the signal intensity under $b > 0$ s/mm^2 and $b = 0$ s/mm^2, respectively. The diffusion data were used to fit the bi-exponential model using a bound-constrained optimization mini-search approach implemented in the MATLAB code[55]. Before the fitting process, a linear fitting was performed on the logarithm of the diffusion data with $1200 > b > 200$ s/mm^2 to generate the D_{slow} parametric map. Furthermore, another internally developed program was employed to extract histogram features of D_{slow}, frac, and D_{fast} from the parametric maps. These features included the 10th and 90th percentile, entropy (a measure of molecular disorder), kurtosis (a measure of the tailedness of a distribution), and skewness (a measure of the asymmetry of a distribution). The processing time per patient was approximately 10 min, including 3 min for ROI drawing in 3D Slicer, 5 min for bi-exponential analysis, and 1 min for histogram feature extraction in MATLAB.

Structural features evaluation

The structural characteristics were assessed by the same neuroradiologist, who was blinded to the patients' initial diagnosis. The tumor site was divided into sub-cortex and deep white matter based on the distance between the tumor body and the cortex. Similar to the previously described method[50], tumors were categorized based on the presence or absence of a peritumoral hyperintense rim on T2-weighted imaging into those with well-defined and blurred margins. The degree of edema was classified as mild, moderate, or severe, according to the criteria proposed in a previous study[56]. Mild edema was defined as hyperintensity on T2-weighted imaging within the radius of the tumor, while severe edema indicated edema extending beyond the diameter of the tumor. Additionally, the classification of enhancement patterns proposed by Wang et al.[57] was used. Focal enhancement was defined as the absence of obvious hyperintensity on T1W + C imaging, with a smooth border and a maximal enhancing focal diameter of < 1.5 cm. Diffuse enhancement was characterized by enhancements with rough edges and maximal diameters > 1.5 cm. Ring-like enhancement was used to describe peripherally enhanced cystic necrosis. No obvious hyperintensity on T1W + C was considered evidence of non-enhancement.

Statistical analysis

Statistical analysis was conducted after confirming the normality and homogeneity of variance. Quantitative variables were presented as mean ± standard deviation and compared using either Student's t-test or Wilcoxon test (Mann-Whitney *U* test). The Chi-square test was employed to compare age and gender. Subsequently, variables that exhibited significant differences were further analyzed using univariate logistic regression, and the best combination model was determined using binary logistic regression. The performance of logistic regression was evaluated using receiver operating characteristic (ROC) analysis, with calculations of the area under the ROC curve (AUC), sensitivity, specificity, positive predictive value (PPV), and negative predictive value (NPV). All statistical analyses were performed using the R software (version 4.0.0). A P-value of < 0.05 was considered statistically significant.

Data availability

The datasets generated and analyzed during the current study are available from the corresponding author upon reasonable request.

References

1. Miller, K. D. et al. Brain and other central nervous system tumor statistics, 2021. *CA Cancer J. Clin.* **71**, 381–406. https://doi.org/10.3322/caac.21693 (2021).
2. Sacks, P. & Rahman, M. Epidemiology of brain metastases. *Neurosurg. Clin. N. Am.* **31**, 481–488. https://doi.org/10.1016/j.nec.2020.06.001 (2020).
3. Louis, D. N. et al. The 2021 WHO classification of tumors of the central nervous system: A summary. *Neuro Oncol.* **23**, 1231–1251. https://doi.org/10.1093/neuonc/noab106 (2021).
4. Horbinski, C. et al. NCCN Guidelines® insights: Central nervous system cancers, Version 2.2022. *J. Natl. Compr. Canc. Netw.* **21**, 12–20. https://doi.org/10.6004/jnccn.2023.0002 (2023).
5. Cha, S. et al. Differentiation of glioblastoma multiforme and single brain metastasis by peak height and percentage of signal intensity recovery derived from dynamic susceptibility-weighted contrast-enhanced perfusion MR imaging. *AJNR Am. J. Neuroradiol.* **28**, 1078–1084. https://doi.org/10.3174/ajnr.A0484 (2007).
6. Chin, H. W., Rasp, G., Kim, J. & Hale, E. R. Role of radiosurgery in the treatment of brain metastasis. *Fed Pract* **32**, 32–37 (2015).
7. Nagai, A., Shibamoto, Y., Yoshida, M., Wakamatsu, K. & Kikuchi, Y. Treatment of single or multiple brain metastases by hypofractionated stereotactic radiotherapy using helical tomotherapy. *Int. J. Mol. Sci.* **15**, 6910–6924. https://doi.org/10.3390/ijms15046910 (2014).
8. Vogelbaum, M. A. et al. Treatment for brain metastases: ASCO-SNO-ASTRO guideline. *J. Clin. Oncol.* **40**, 492–516. https://doi.org/10.1200/JCO.21.02314 (2022).
9. Faehndrich, J. et al. Neuroradiological viewpoint on the diagnostics of space-occupying brain lesions. *Clin. Neuroradiol.* **21**, 123–139. https://doi.org/10.1007/s00062-011-0073-6 (2011).
10. Elmariah, S. B., Huse, J., Mason, B., Leroux, P. & Lustig, R. A. Multicentric glioblastoma multiforme in a patient with BRCA-1 invasive breast cancer. *Breast J.* **12**, 470–474. https://doi.org/10.1111/j.1075-122X.2006.00307.x (2006).
11. Davis, F. G. et al. Glioblastoma incidence rate trends in Canada and the United States compared with England, 1995–2015. *Neuro Oncol.* **22**, 301–302. https://doi.org/10.1093/neuonc/noz203 (2020).
12. Arévalo-Sáenz, A., Rodríguez-Boto Amago, G. & Pedrosa Sánchez, M. High-grade glioma and solitary metastasis: Differentiation by spectroscopy and advanced magnetic resonance techniques. *Egypt. J. Neurosurg.* **37**, 34. https://doi.org/10.1186/s41984-022-00172-y (2022).

13. Schwartz, K. M., Erickson, B. J. & Lucchinetti, C. Pattern of T2 hypointensity associated with ring-enhancing brain lesions can help to differentiate pathology. *Neuroradiology* **48**, 143–149. https://doi.org/10.1007/s00234-005-0024-5 (2006).

14. Baris, M. M., Celik, A. O., Gezer, N. S. & Ada, E. Role of mass effect, tumor volume and peritumoral edema volume in the differential diagnosis of primary brain tumor and metastasis. *Clin. Neurol. Neurosurg.* **148**, 67–71. https://doi.org/10.1016/j.clineuro.2016.07.008 (2016).

15. Zhang, G. et al. Discrimination between solitary brain metastasis and glioblastoma multiforme by using ADC-based texture analysis: A comparison of two different ROI placements. *Acad. Radiol.* **26**, 1466–1472. https://doi.org/10.1016/j.acra.2019.01.010 (2019).

16. Gao, E. et al. Histogram analysis based on diffusion kurtosis imaging: Differentiating glioblastoma multiforme from single brain metastasis and comparing the diagnostic performance of two region of interest placements. *Eur. J. Radiol.* **147**, 110104. https://doi.org/10.1016/j.ejrad.2021.110104 (2022).

17. Voicu, I. P. et al. Differentiating solitary brain metastases from high-grade gliomas with MR: Comparing qualitative versus quantitative diagnostic strategies. *Radiol. Med.* **127**, 891–898. https://doi.org/10.1007/s11547-022-01516-2 (2022).

18. Suh, C. H., Kim, H. S., Jung, S. C., Choi, C. G. & Kim, S. J. Perfusion MRI as a diagnostic biomarker for differentiating glioma from brain metastasis: A systematic review and meta-analysis. *Eur. Radiol.* **28**, 3819–3831. https://doi.org/10.1007/s00330-018-5335-0 (2018).

19. Le Bihan, D. & Turner, R. The capillary network: A link between IVIM and classical perfusion. *Magn. Reson. Med.* **27**, 171–178. https://doi.org/10.1002/mrm.1910270116 (1992).

20. Kusunoki, M. et al. Differentiation of high-grade from low-grade diffuse gliomas using diffusion-weighted imaging: A comparative study of mono-, bi-, and stretched-exponential diffusion models. *Neuroradiology* **62**, 815–823. https://doi.org/10.1007/s00234-020-02456-2 (2020).

21. Nguyen, D. H. et al. Discriminating glioblastoma from solitary brain metastases on 3 Tesla magnetic resonance imaging: The roles of fractional anisotropy and mean diffusivity. *Eur. Rev. Med. Pharmacol. Sci.* **26**, 8823–8831. https://doi.org/10.26355/eurrev_202212_30554 (2022).

22. Heynold, E. et al. Physiological MRI biomarkers in the differentiation between glioblastomas and solitary brain metastases. *Mol. Imaging Biol.* **23**, 787–795. https://doi.org/10.1007/s11307-021-01604-1 (2021).

23. Li, X. et al. Discrimination between glioblastoma and solitary brain metastasis: Comparison of inflow-based vascular-space-occupancy and dynamic susceptibility contrast MR imaging. *AJNR Am J. Neuroradiol.* **41**, 583–590. https://doi.org/10.3174/ajnr.A6466 (2020).

24. Qin, J., Li, Y., Liang, D., Zhang, Y. & Yao, W. Histogram analysis of absolute cerebral blood volume map can distinguish glioblastoma from solitary brain metastasis. *Medicine (Baltimore)* **98**, e17515. https://doi.org/10.1097/md.0000000000017515 (2019).

25. Romano, A. et al. Single brain metastasis versus glioblastoma multiforme: A VOI-based multiparametric analysis for differential diagnosis. *Radiol. Med.* **127**, 490–497. https://doi.org/10.1007/s11547-022-01480-x (2022).

26. Markwell, S. M., Ross, J. L., Olson, C. L. & Brat, D. J. Necrotic reshaping of the glioma microenvironment drives disease progression. *Acta Neuropathol.* **143**, 291–310. https://doi.org/10.1007/s00401-021-02401-4 (2022).

27. Poulon, F. et al. Real-time Brain Tumor imaging with endogenous fluorophores: A diagnosis proof-of-concept study on fresh human samples. *Sci. Rep.* **8**, 14888. https://doi.org/10.1038/s41598-018-33134-2 (2018).

28. Chiang, I. C. et al. Distinction between high-grade gliomas and solitary metastases using peritumoral 3-T magnetic resonance spectroscopy, diffusion, and perfusion imagings. *Neuroradiology* **46**, 619–627. https://doi.org/10.1007/s00234-004-1246-7 (2004).

29. Tsougos, I. et al. Differentiation of glioblastoma multiforme from metastatic brain tumor using proton magnetic resonance spectroscopy, diffusion and perfusion metrics at 3 T. *Cancer Imaging* **12**, 423–436. https://doi.org/10.1102/1470-7330.2012.0038 (2012).

30. Cha, S. et al. Intracranial mass lesions: Dynamic contrast-enhanced susceptibility-weighted echo-planar perfusion MR imaging. *Radiology* **223**, 11–29. https://doi.org/10.1148/radiol.2231010594 (2002).

31. Pons-Escoda, A. et al. Voxel-level analysis of normalized DSC-PWI time-intensity curves: A potential generalizable approach and its proof of concept in discriminating glioblastoma and metastasis. *Eur. Radiol.* **32**, 3705–3715. https://doi.org/10.1007/s00330-021-08498-1 (2022).

32. She, D., Xing, Z. & Cao, D. Differentiation of glioblastoma and solitary brain metastasis by gradient of relative cerebral blood volume in the peritumoral brain zone derived from dynamic susceptibility contrast perfusion magnetic resonance imaging. *J. Comput. Assist. Tomogr.* **43**, 13–17. https://doi.org/10.1097/rct.0000000000000771 (2019).

33. Aparici-Robles, F. et al. Glioblastoma versus solitary brain metastasis: MRI differentiation using the edema perfusion gradient. *J. Neuroimaging* **32**, 127–133. https://doi.org/10.1111/jon.12920 (2022).

34. Auffinger, B., Spencer, D., Pytel, P., Ahmed, A. U. & Lesniak, M. S. The role of glioma stem cells in chemotherapy resistance and glioblastoma multiforme recurrence. *Expert. Rev. Neurother.* **15**, 741–752. https://doi.org/10.1586/14737175.2015.1051968 (2015).

35. Jackson, M., Hassiotou, F. & Nowak, A. Glioblastoma stem-like cells: At the root of tumor recurrence and a therapeutic target. *Carcinogenesis* **36**, 177–185. https://doi.org/10.1093/carcin/bgu243 (2015).

36. Blecharz, K. G., Colla, R., Rohde, V. & Vajkoczy, P. Control of the blood-brain barrier function in cancer cell metastasis. *Biol. Cell* **107**, 342–371. https://doi.org/10.1111/boc.201500011 (2015).

37. Wang, C. et al. Distribution of intravoxel incoherent motion MRI-related parameters in the brain: evidence of interhemispheric asymmetry. *Clin. Radiol.* **72**(94), e91-94.e96. https://doi.org/10.1016/j.crad.2016.09.007 (2017).

38. Willemse, J. R. J. et al. Identifying the primary tumour in patients with cancer of unknown primary (CUP) using [(18)F]FDG PET/CT: A systematic review and individual patient data meta-analysis. *Eur. J. Nucl. Med. Mol. Imaging* https://doi.org/10.1007/s00259-024-06860-1 (2024).

39. Aslan, K., Gunbey, H. P., Tomak, L. & Incesu, L. Multiparametric MRI in differentiating solitary brain metastasis from high-grade glioma: Diagnostic value of the combined use of diffusion-weighted imaging, dynamic susceptibility contrast imaging, and magnetic resonance spectroscopy parameters. *Neurol. Neurochir. Pol.* **53**, 227–237. https://doi.org/10.5603/PJNNS.a2019.0024 (2019).

40. Kuett, L. et al. Distant metastases of breast cancer resemble primary tumors in cancer cell composition but differ in immune cell phenotypes. *Cancer Res.* https://doi.org/10.1158/0008-5472.Can-24-1211 (2024).

41. Fioni, F., Chen, S. J., Lister, I. N. E., Ghalwash, A. A. & Long, M. Z. Differentiation of high grade glioma and solitary brain metastases by measuring relative cerebral blood volume and fractional anisotropy: A systematic review and meta-analysis of MRI diagnostic test accuracy studies. *Br. J. Radiol.* **96**, 20220052. https://doi.org/10.1259/bjr.20220052 (2023).

42. Iima, M. & Le Bihan, D. Clinical intravoxel incoherent motion and diffusion MR imaging: Past, present, and future. *Radiology* **278**, 13–32. https://doi.org/10.1148/radiol.2015150244 (2016).

43. Chabert, S. et al. Impact of b-value sampling scheme on brain ivim parameter estimation in healthy subjects. *Magn. Reson. Med. Sci.* **19**, 216–226. https://doi.org/10.2463/mrms.mp.2019-0061 (2020).

44. Wang, C. et al. Distribution of intravoxel incoherent motion MRI-related parameters in the brain: evidence of interhemispheric asymmetry. *Clin. Radiol.* **72**, e91–e96. https://doi.org/10.1016/j.crad.2016.09.007 (2017).

45. Han, C., Huang, S., Guo, J., Zhuang, X. & Han, H. Use of a high b-value for diffusion weighted imaging of peritumoral regions to differentiate high-grade gliomas and solitary metastases. *J. Magn. Reson. Imaging* **42**, 80–86. https://doi.org/10.1002/jmri.24747 (2015).

11

46. Pavilla, A. et al. Intravoxel incoherent motion and diffusion kurtosis imaging at 3T MRI: Application to ischemic stroke. *Magn. Reson. Imaging* **99**, 73–80. https://doi.org/10.1016/j.mri.2023.01.018 (2023).
47. Pavilla, A. et al. Measuring cerebral hypoperfusion induced by hyperventilation challenge with intravoxel incoherent motion magnetic resonance imaging in healthy volunteers. *J. Comput. Assist. Tomogr.* **42**, 85–91. https://doi.org/10.1097/RCT.0000000000000640 (2018).
48. Bai, J. et al. High-performance presurgical differentiation of glioblastoma and metastasis by means of multiparametric neurite orientation dispersion and density imaging (NODDI) radiomics. *Eur. Radiol.* **34**, 6616–6628. https://doi.org/10.1007/s00330-024-10686-8 (2024).
49. Xiong, Z. et al. Deep learning models for rapid discrimination of high-grade gliomas from solitary brain metastases using multi-plane T1-weighted contrast-enhanced (T1CE) images. *Quant. Imaging Med. Surg.* **14**, 5762–5773. https://doi.org/10.21037/qims-24-380 (2024).
50. Yamamoto, J. et al. Evaluation of peritumoral brain parenchyma using contrast-enhanced 3D fast imaging employing steady-state acquisition at 3T for differentiating metastatic brain tumors and glioblastomas. *World Neurosurg.* **120**, e719–e729. https://doi.org/10.1016/j.wneu.2018.08.147 (2018).
51. Otman, H. *Artificial Intelligence Improves Brain Tumor Diagnosis*, https://www.michiganmedicine.org/health-lab/artificial-intelligence-improves-brain-tumor-diagnosis (2020).
52. Louis, D. N. et al. The 2016 World Health Organization classification of tumors of the central nervous system: A summary. *Acta Neuropathol.* **131**, 803–820. https://doi.org/10.1007/s00401-016-1545-1 (2016).
53. Yu, H. et al. Applying protein-based amide proton transfer MR imaging to distinguish solitary brain metastases from glioblastoma. *Eur. Radiol.* **27**, 4516–4524. https://doi.org/10.1007/s00330-017-4867-z (2017).
54. Kim, M. et al. Diffusion- and perfusion-weighted MRI radiomics model may predict isocitrate dehydrogenase (IDH) mutation and tumor aggressiveness in diffuse lower grade glioma. *Eur. Radiol.* **30**, 2142–2151. https://doi.org/10.1007/s00330-019-06548-3 (2020).
55. D'Errico, J. *fminsearchbnd, fminsearchcon*, https://www.mathworks.com/matlabcentral/fileexchange/8277-fminsearchbnd-fminsearchcon (2023).
56. Pope, W. B. et al. MR imaging correlates of survival in patients with high-grade gliomas. *AJNR Am. J. Neuroradiol.* **26**, 2466–2474 (2005).
57. Wang, Y. et al. Identifying the association between contrast enhancement pattern, surgical resection, and prognosis in anaplastic glioma patients. *Neuroradiology* **58**, 367–374. https://doi.org/10.1007/s00234-016-1640-y (2016).

Acknowledgements

Author contributions
Conceptualization: Hongming Ji, Cheng Xu, and Rui Cheng. Methodology: Jinxia Guo and Yifei Su. Formal analysis and investigation: Yifei Su, Junhao Wang, and Jinxia Guo. Writing - original draft preparation: Yifei Su and Junhao Wang. Writing - review and editing: Jinxia Guo and Chunhong Wang. Funding acquisition: none. Resources: Yifei Su, Junhao Wang, Xuanchen Liu, and Xiaoxiong Yang. Supervision: Hongming Ji and Cheng Xu. All authors approved the version to be published and agreed to be accountable for all aspects of the work to ensure that questions related to the accuracy or integrity of any part of the work are appropriately investigated and resolved.

Funding
The authors did not receive support from any organization for the submitted work.

Declarations

Competing interests
J. Guo is an employee of GE Healthcare. The other authors have no conflicts of interest to declare.

Ethics approval
The study was conducted in accordance with the Declaration of Helsinki (as revised in 2013). The protocol was reviewed and approved by the Ethics Committee of Shanxi Provincial People's Hospital/Fifth Hospital of Shanxi Medical University (2022 Research Review No. 153).

Consent to participate
The informed consent was waived by the Ethics Committee of Shanxi Provincial People's Hospital /Fifth Hospital of Shanxi Medical University (2022 Research Review No. 153).

Consent to publish
Not applicable.

Additional information
Supplementary Information The online version contains supplementary material available at https://doi.org/10.1038/s41598-024-83452-x.

Correspondence and requests for materials should be addressed to H.J.

Reprints and permissions information is available at www.nature.com/reprints.

Publisher's note Springer Nature remains neutral with regard to jurisdictional claims in published maps and institutional affiliations.